

How Can We Decrease Defect Density in Si Multicrystals to Realize High-Efficiency Solar Cells?

To manipulate crystal defects and impurities in Si multicrystals is a promising route to improve conversion efficiency of solar cells. Therefore, development of a novel crystal growth technique to permit artificial control of defects has been pursued. It would be ideal if such a technique is based on the practical directional solidification. For this purpose, fundamental understanding of mechanisms on generation of defects during crystal growth is of crucial importance so that one can answer an open question, "How can we decrease defect density in Si multicrystals?"

In order to answer the question, we started with model crystal growth experiments using a seed crystal to consist of a couple of single crystals with an artificially controlled grain boundary configuration, namely $\langle 110 \rangle$ tilt grain boundary. Spatially resolved X-ray rocking curve analysis and evaluation of etch-pit density clarified that "sub-grain boundaries", which consist of a cluster of dislocations and give detrimental effect on solar cell performance, are generated from the grain boundary as crystal growth proceeds. Furthermore, the amount of dislocations was found to be strongly dependent on the grain boundary configuration. In a particular configuration, dislocations were mostly localized in one of the grains to consist of a grain boundary [1].

Since Si expands when crystallized from the melt, compressive stress is supposed to be applied owing to the contact with a rigid crucible. This led us to assume that local shear stress around a grain boundary, which would depend on the configuration of the grain boundary, might explain the experimentally observed difference in defect density. To see if this hypothesis is reasonable, we carried out three-dimensional finite element analysis of shear stress for a model bi-crystal with a single grain boundary. By taking anisotropic elastic constants into account, calculations were performed for various grain boundary configurations. Interestingly, dislocation density was found to be well correlated with the calculated local shear stress around the grain boundary. The shear stress is likely to be reduced when

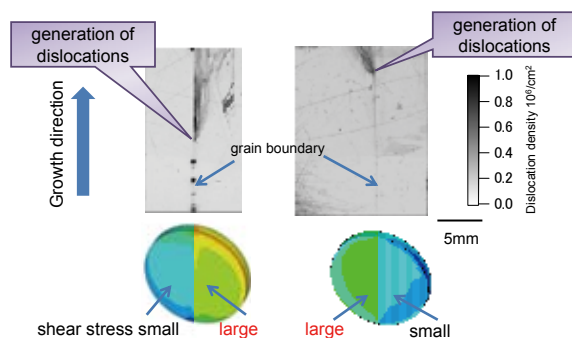


Fig. 1 Spatial distribution of dislocations in model crystals grown using seeds with controlled grain boundary configuration, and shear stress distribution calculated by finite element analysis. It is clearly seen that dislocations are generated from grain boundaries and localized at one of the crystal grains with larger shear stress.

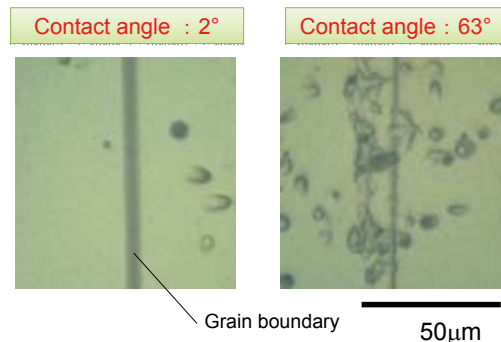


Fig. 2 Comparison of dislocation density around grain boundaries with different contact angles of adjacent dendrite crystals. It is seen that parallel contact is favorable in terms of reduction of dislocations.

the rotational symmetry is improved along the direction perpendicular to the plane where external stress from the crucible is introduced.

This knowledge inspired us to suppress dislocations during directional solidification by controlling the coherency of the grain boundary without any seeds so that one could decrease shear stress around the grain boundary.

The attempt to change the coherency of the grain boundary was made by utilizing nucleation of plural dendrite crystals. Since the upper plane of the dendrite crystal can be limited to either $\{110\}$ or $\{112\}$, the coherency of the grain boundary can be controlled by the contact angle between adjacent dendrite crystals. Crystal growth was started with dendritic nucleation by establishing the amount of supercooling larger than 10 K. The contact angle was measured by using electron back scattering pattern analysis. Dislocation density measured by counting etch-pits revealed that parallel contact of adjacent dendrite crystals is useful to suppress generation of dislocations. On the other hand, increase of the contact angle resulted in increase of the dislocation density. This confirms that control of the coherency of grain boundaries at the initial stage is very important for decreasing dislocations in the whole ingot [2].

References

- [1] I. Takahashi, N. Usami, K. Kutsukake, G. Stokkan, K. Morishita, and K. Nakajima, *J. Cryst. Growth* **312**, 897-901 (2010).
- [2] N. Usami, R. Yokoyama, I. Takahashi, K. Kutsukake, K. Fujiwara, and K. Nakajima, *J. Appl. Phys.* **107**, 013511 (2010).

Key Words

Dislocation, Grain Boundary, Dendrite

Contact to

Noritaka Usami (Crystal Physics Division)

E-mail: usa@imr.tohoku.ac.jp

URL: <http://www.xtalphys.imr.tohoku.ac.jp>

Phase Stability of Metallic Nano-Clusters Studied by Positron 2D-ACAR : Fermi Surface - Brillouin Zone Interactions

A general approach is outlined to predict the chemical compositions of solute nano-clusters embedded in materials with nearly free electrons. Based on the experimental results of the two-dimensional angular correlation of positron annihilation radiation (2D-ACAR) and the corresponding theoretical calculations, we show that the Fermi surface - Brillouin zone interaction is a key to understand the chemical composition realized in solute nano-clusters. This concept is also useful to understand the stability of impurity clusters formed in nuclear materials by irradiation.

It is well known that a positron, an antiparticle of an electron, is a sensitive probe of open volume defects because it can be trapped in the defects and then annihilates there with the surrounding electron conveying significant information on the electronic environment around the defect site with the emitted two gamma-rays. However, we recently found that a positron can be also trapped in solute nano-clusters with positron affinities higher than that of matrix even if the nano-clusters are free from the open volume defects. We named this phenomenon quantum positron confinement. [1]. Using the quantum positron confinement, we can reveal electronic structure of the solute nano-clusters by two-dimensional angular correlation of positron annihilation radiation (2D-ACAR) method [2].

As an example, Fig. 1 shows the anisotropies of electron momentum distributions in Ag and Zn clusters in Al experimentally obtained by 2D-ACAR method [3]. We can discuss the Fermi surface topology of the solute nano-clusters from the 2D-ACAR anisotropies. By comparing with the theoretical calculations shown in Fig. 2, the chemical compositions (electron/atom ratios) in the solute nano-clusters are determined. The Ag cluster is close to Al:Ag=1:3 and the Zn cluster is almost pure Zn.

Based on these results, we proposed a general rule to suggest preferential chemical composition of solute nano-clusters coherent to matrix with nearly free electrons. The Fermi surface - Brillouin zone interaction is a key to understand the chemical composition realized in the solute nano-clusters because the presence of necks on the Fermi surface contributes to the reduction in the total electron energy due to the band gap effect.

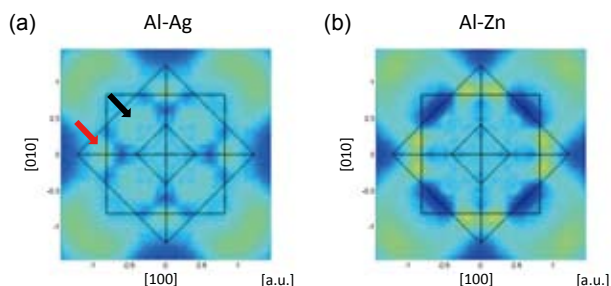


Fig. 1 3D plots of experimental 2D-ACAR anisotropies projected along the [100] direction for (a) Ag cluster in Al and (b) Zn cluster in Al.

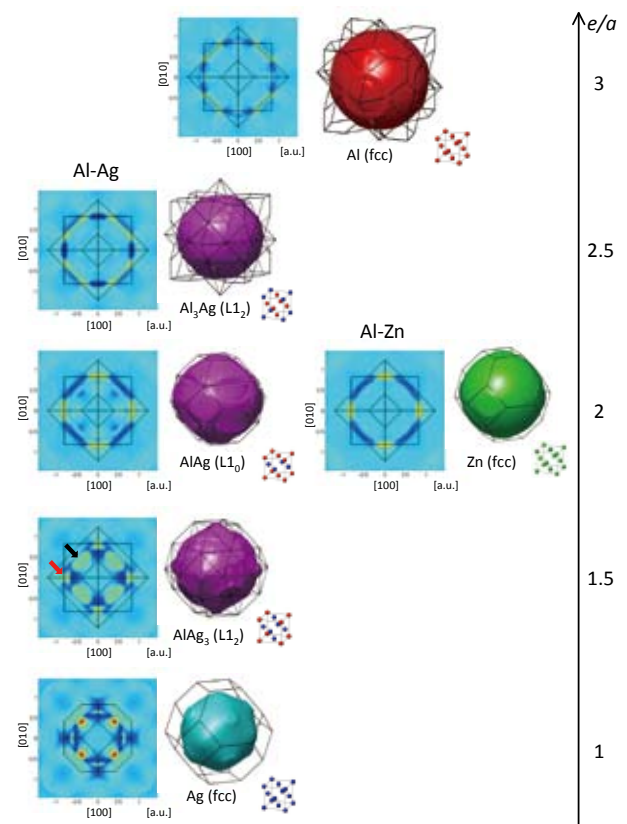


Fig. 2 3D plots of calculated 2D-ACAR anisotropies projected along the [100] direction and Fermi surfaces by FLAPW calculations for pure Al, Al₃Ag, AlAg, AlAg₃, pure Ag, and pure Zn (fcc).

References

- [1] Y. Nagai, M. Hasegawa, Z. Tang, A. Hempel, K. Yubuta, T. Shimamura, Y. Kawazoe, A. Kawai, and F. Kano, Phys. Rev. B **61**, 6574 (2000).
- [2] Y. Nagai, T. Chiba, Z. Tang, T. Akahane, T. Kanai, M. Hasegawa, M. Takenaka, and E. Kuramoto, Phys. Rev. Lett. **87**, 176402 (2001).
- [3] Y. Nagai, T. Toyama, Z. Tang, K. Inoue, T. Chiba, M. Hasegawa, S. Hirose, and T. Sato: Phys. Rev. B **79**, 201405(R) (2009).

Key Words

Embedded Nanoparticle, Positron Annihilation, Fermi Surface

Contact to

Yasuyoshi Nagai (Irradiation Effects in Nuclear and Their Related Materials Division)

E-mail: nagai@imr.tohoku.ac.jp

URL: <http://wani.imr.tohoku.ac.jp/>

Hydrogen Incorporation and Optical Absorption of Tungsten Oxide Films

Ion-beam analysis techniques combined with optical detection can provide useful non-destructive and in-situ observation of retention and transport behavior of hydrogen in nuclear materials. We demonstrate simultaneous measurements of optical absorption and hydrogen concentration in tungsten oxide films under gas exposure and/or ion implantation, to reveal the coloration phenomena accompanied with an insertion of hydrogen in the tungsten tri-oxide film.

In near-term fusion devices such as ITER (International Thermonuclear Experimental Reactor), tungsten is a candidate material for plasma facing components because of its superior physical and mechanical properties at high temperature. Although the pure tungsten metal shows very little solubility of hydrogen, re-deposited layer on the first wall surface can contain carbides and oxides, retaining hydrogen isotopes up to considerably high concentration. It is essentially important to clarify the transport behavior of hydrogen isotopes in the first wall surface to control fuel balance and tritium inventory. On the other hand, it is known that tungsten tri-oxide films covered with a thin catalyst layer show a reversible coloration phenomenon under hydrogen exposure. Because the hydrogen gas has a relatively low explosive limit in the atmosphere, development of a sensor of hydrogen gas is also important to handle hydrogen safely. The mechanism of this gasochromic phenomenon is not fully understood, while the optical characteristic of the tungsten oxide film was investigated by electrochemical techniques and by infrared absorption

Recently, we demonstrated that hydrogen atoms were incorporated in the WO₃ film during the gasochromic coloration by direct measurement of hydrogen concentration in the film using the ion beam analysis technique combined with optical measurements as shown in Fig. 1 [1]. Tungsten oxide thin films were prepared on a SiO₂ glass substrates by a reactive RF magnetron sputtering using a metal W target. The concentration depth profiles of hydrogen in the near surface layer were measured by the Elastic Recoil Detection Analysis (ERDA) technique, performed in a scattering vacuum chamber which was connected to a 1.7 MV tandem accelerator. The optical transmittance was simultaneously measured by a CCD camera equipped with a monochromator. It was clearly observed that the hydrogen concentration in

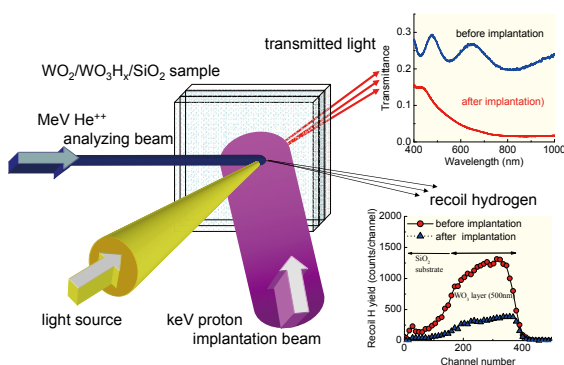


Fig. 1 Schematics of the simultaneous measurement system for hydrogen concentration and optical absorption of tungsten oxide films. During the keV H⁺ ion implantation into surface layer, energies of hydrogen recoiled by MeV He ions are analyzed, and a transmitted light spectrum is obtained.

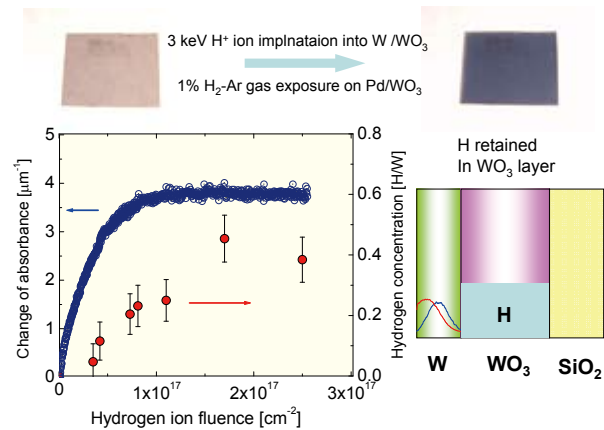


Fig. 2 Absorption coefficient and retained hydrogen concentration in the sandwiched WO₃ layer, plotted as a function of incident 3 keV H⁺ ions. The photo-images of Pd/WO₃/SiO₂ sample as prepared and exposed by 1%H₂-Ar mixture gas are inserted in upper part.

the film increased with the coloring process. The evidence of the coloration accompanied by the hydrogen incorporation supports the double injection model, in which protons and electrons are simultaneously inserted into a WO₃ film to reduce WO⁶⁺ to WO⁵⁺. The relation between hydrogen and coloration has been further analyzed under ion implantation, and structural and compositional effects on the optical properties were systematically analyzed to optimize the preparation condition of the films [2].

Figure 2 shows changes of optical absorption in the wavelengths between 600 and 900 nm of W/WO₃/SiO₂ sample, and hydrogen retention in the sandwiched WO₃ layer under 3 keV H⁺ ion implantation at a room temperature. Because the incident H ion totally loses its energy in the W layer, no damage was created in the sandwiched WO₃ layer. At the beginning of the implantation, nearly 100 % hydrogen atoms implanted in the W layer diffused into the WO₃ layer and were retained, accompanied with coloration of the WO₃ layer. The coloration was completed at the fluence of about 1x10¹⁷ cm⁻², corresponding to the increase of the H concentration about 0.2 H/W. The evaluated coloration efficiency about 40 cm²C⁻¹ was fairly consistent with the previous experiment under Ar-H₂ gas exposure [1], indicating that mechanism of the ion implantation induced coloration is the same as the gasochromic phenomenon.

References

- [1] S. Nagata, A. Inouye, S. Yamamoto, B. Tsuchiya, K. Takano, K. Toh and T. Shikama, J. Alloys and Comp. **446-447**, 558 (2007).
- [2] A. Inouye, S. Yamamoto, S. Nagata, M. Yoshikawa and T. Shikama, Nucl. Instr. and Meth. **B 267**, 1480 (2009).

Key Words

Tungsten Oxides, Ion-beam, Optical Absorption

Contact to

Shinji Nagata (Nuclear Materials Science Division)
E-mail: nagata@imr.tohoku.ac.jp

In-situ TEM Observation and First Principle Calculation Study on Hydride Formation in Zirconium Alloy

The growth process of Zr hydride in Zircaloy-4 was investigated using in-situ TEM observations under implantation with hydrogen ions followed by molecular dynamics and first principle calculations so as to clarify the formation mechanism. Stacking fault associated with partial dislocations on the hydride is presumed to have an important role for the formation.

The mechanical degradations of zircaloy claddings in LWRs strongly depend on distribution of hydrides because of their characteristics in mechanical properties. Therefore, it is important to understand the formation mechanism of Zr hydride to control the behavior of embrittlement of cladding materials [1].

In this study, we investigated the formation of Zr hydrides associated with dislocations both by electron microscopy, molecular dynamics and first principle calculations.

1. In-situ TEM observations of Zr hydride under hydrogen ion implantation

In-situ observations during hydrogen ion implantation were performed with a TEM interfaced with an ion accelerator. In electron transparent thin foils, low density of hydrides were introduced during electrochemical polishing. Growth processes of Zr hydrides accompanied by the formation of dislocations were observed simultaneously under irradiation with 150-keV H_2^+ ions at room temperature as shown in Fig. 1. The crystallographic relationship between the Zr matrix and Zr hydrides was identical with the previous studies. The direction of growth was in the direction. Dislocations were formed at the tip of hydrides. The contrast implied they were extended into partial dislocations. The distance between them were less than 5 nm and 20nm, respectively, in Zr matrix and at a tip of hydrides.

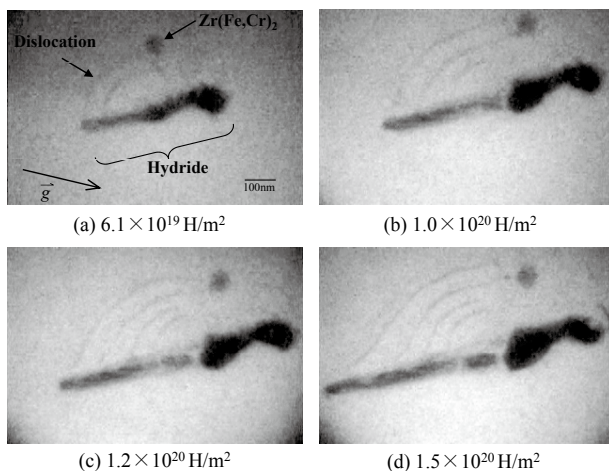


Fig. 1 The preferential growth of zirconium hydride along under 150-keV H_2^+ ions at room temperature.

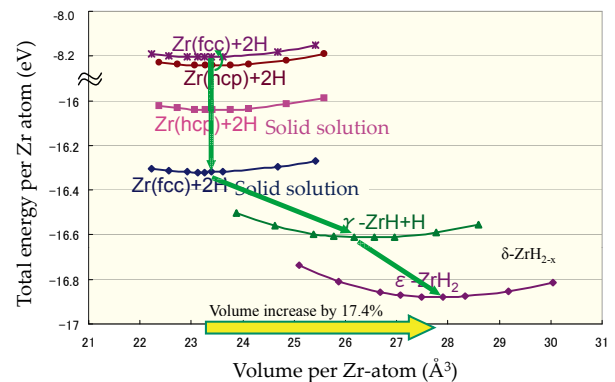


Fig. 2 First principle calculation of zirconium hydrides compared with pure zirconium.

2. Modeling for hydride formation

Molecular dynamics simulation was performed to represent the formation of partial dislocations which are extended from a basal dislocation and roughly 4 nm apart, well agree with the experimental results, and suggest fairly low stacking fault energy in hydride. The first principle calculations employing VASP 4.6 code was applied to the Zr-H system to clarify (1) stability of Zr-H solid solution, (2) preferable crystal plane of H atoms and (3) stable Zr hydride crystal. As shown in Fig. 2, it is concluded that lower energy was achieved in Zr (fcc)-H solid solution than Zr (hcp)-H, and ϵ or δ -ZrH₂ is the stable intermetallic compound among possible allotropes. Accumulation of hydrogen at partial dislocations is presumably attributable for the hydride formation.

References

[1] H. Abe, Japan/Korea Joint Seminar, Annual Meeting of Atomic Energy Society of Japan Sept 16, 2009, Tohoku University

Key Words

Zirconium, Hydrogen Implantation, Transmission Electron Microscope

Contact to

Hiroaki Abe (Nuclear Materials Engineering Division)

E-mail: abe.hiroaki@imr.tohoku.ac.jp

URL: <http://www-lab.imr.tohoku.ac.jp/~abeken/>

Complex Hydrides with $(\text{BH}_4)^-$ and $(\text{NH}_2)^-$ Anions as New Lithium Fast-Ion Conductors

We have studied lithium ion conductivities of complex hydrides $\text{Li}_2(\text{BH}_4)(\text{NH}_2)$ and $\text{Li}_4(\text{BH}_4)(\text{NH}_2)_3$, both with combinations of the $(\text{BH}_4)^-$ and $(\text{NH}_2)^-$ anions. Ac impedance measurements demonstrate that both $\text{Li}_2(\text{BH}_4)(\text{NH}_2)$ and $\text{Li}_4(\text{BH}_4)(\text{NH}_2)_3$ are novel lithium fast-ion conductors (2×10^{-4} S/cm at room temperature) due to being provided new occupation sites for Li^+ ions.

We have recently reported that a complex hydride $\text{Li}(\text{BH}_4)$, a potential candidate for advanced hydrogen storage materials [1], exhibits lithium fast-ion conduction (10^{-3} S/cm) due to its structural transition at 390 K [2]. Research and development of lithium (fast-)ion conductors is significantly important because they can be potentially used as solid electrolytes in all-solid-state lithium ion batteries. From the application point of view, it is highly desirable to enhance the conductivity of $\text{Li}(\text{BH}_4)$ at room temperature (RT).

Figure 1 shows the temperature dependences of the electrical conductivities of $\text{Li}_2(\text{BH}_4)(\text{NH}_2)$ and $\text{Li}_4(\text{BH}_4)(\text{NH}_2)_3$ [3]. $\text{Li}_2(\text{BH}_4)(\text{NH}_2)$ exhibits fast-ion conductivity of 2×10^{-4} S/cm at RT, which is four and five orders of magnitude higher than those of the host hydrides $\text{Li}(\text{BH}_4)$ and $\text{Li}(\text{NH}_2)$, respectively, and the conductivity monotonically increases upon heating. The activation energy for conduction significantly decreases at around 368 K from 0.56 eV (303–348 K) to 0.24 eV (above 368 K). This significant change in the activation energy is attributed to the melting of $\text{Li}_2(\text{BH}_4)(\text{NH}_2)$. The total ion conductivity reaches up to 6×10^{-2} S/cm after melting at the highest temperature measured (378 K). $\text{Li}_4(\text{BH}_4)(\text{NH}_2)_3$ also exhibits fast ion conductivities of 2×10^{-4} S/cm even at RT. The activation energy for conduction is evaluated to be 0.26 eV, which is less than half that in $\text{Li}_2(\text{BH}_4)(\text{NH}_2)$ before melting and $\text{Li}(\text{BH}_4)$, indicating the higher mobility of Li^+ ions.

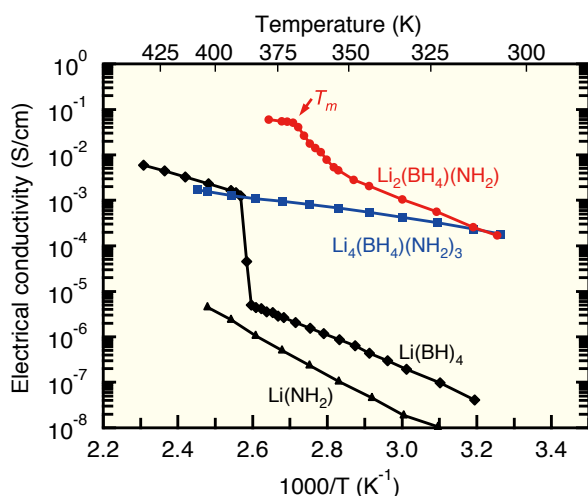


Fig. 1 Temperature dependences of the electrical conductivity of $\text{Li}_2(\text{BH}_4)(\text{NH}_2)$ and $\text{Li}_4(\text{BH}_4)(\text{NH}_2)_3$. The melting temperature of $\text{Li}_2(\text{BH}_4)(\text{NH}_2)$, 365 K, is indicated as T_m . For reference, the data of $\text{Li}(\text{BH}_4)$ and $\text{Li}(\text{NH}_2)$ as host hydrides are also shown.

As shown in Fig. 2, both $\text{Li}_2(\text{BH}_4)(\text{NH}_2)$ and $\text{Li}_4(\text{BH}_4)(\text{NH}_2)_3$ have plural occupation sites for Li^+ ions with different tetrahedral coordination sites consisting of $(\text{BH}_4)^-$ and $(\text{NH}_2)^-$ anions. $\text{Li}_2(\text{BH}_4)(\text{NH}_2)$ has eighteen $\text{Li}(1)$ s and eighteen $\text{Li}(2)$ s per unit cell while $\text{Li}_4(\text{BH}_4)(\text{NH}_2)_3$ has twelve $\text{Li}(1)$ s, twelve $\text{Li}(2)$ s and eight $\text{Li}(3)$ s. Calculation of the size of the each occupation site (one good factor to estimate the size of the bottleneck for Li^+ ion diffusion) demonstrates that 50% Li^+ ions occupy the rather small $\text{Li}(2)$ (approximately 56% in radius and 18% in volume of the $\text{Li}(1)$) in $\text{Li}_2(\text{BH}_4)(\text{NH}_2)$. The larger activation energy for conduction for $\text{Li}_2(\text{BH}_4)(\text{NH}_2)$ than for $\text{Li}_4(\text{BH}_4)(\text{NH}_2)_3$ can be explained by the Li^+ ions with lower mobility in the smaller $\text{Li}(2)$.

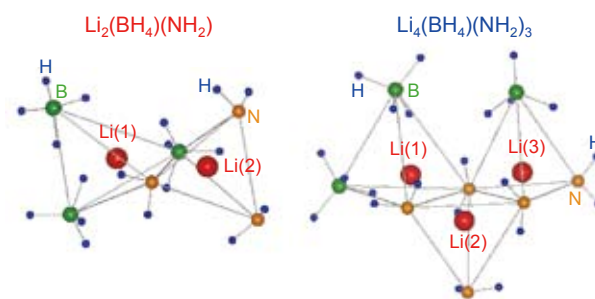


Fig. 2 Local atomic structures of $\text{Li}_2(\text{BH}_4)(\text{NH}_2)$ and $\text{Li}_4(\text{BH}_4)(\text{NH}_2)_3$. Red, green, orange and blue solid circles show Li, B, N and H, respectively.

References

- [1] S. Orimo, Y. Nakamori, J.R. Eliseo, A. Züttel and C.M. Jensen, Chem. Rev., **107**, 4111 (2007).
- [2] M. Matsuo, Y. Nakamori, S. Orimo, H. Maekawa and H. Takamura, Appl. Phys. Lett., **91**, 224103 (2007).
- [3] M. Matsuo, A. Remhof, P. Martelli, R. Caputo, M. Ernst, Y. Miura, T. Sato, H. Oguchi, H. Maekawa, H. Takamura, A. Borgschulte, A. Züttel and S. Orimo, J. Am. Chem. Soc., **131**, 16389 (2009).

Key Words

Complex Hydride, Lithium Fast-Ion Conductor, Solid Electrolyte

Contact to

Shin-ichi Orimo (Hydrogen Functional Materials Division)

E-mail: orimo@imr.tohoku.ac.jp

URL: <http://www.hydrogen.imr.tohoku.ac.jp>

Hydrothermal Synthesis of Actinide Dioxides for Fabrication and Reprocessing of MOX Nuclear Fuel

We have recently focused on application of hydrothermal synthesis of actinide dioxides for fabrication and reprocessing of MOX fuel in order to improve the nuclear fuel cycle much simpler and safer. This process enables us to reduce amounts of radioactive wastes and possible risks of fire and/or explosion, and also to control various specifications of the MOX fuel.

The small emission of carbon dioxide from the nuclear power generation has made it attractive energy sources. In the commercial nuclear power plants, uranium dioxides or the solid solution with plutonium dioxides, *i.e.* so-called the "mixed oxides" (MOX), with fluorite-structure have been used exclusively because of the high melting point (>2800°C). However, the fuel fabrication consists of complicated solid-chemical processes including a precipitation from solution, its calcination followed by H₂ reduction, and crush and granulation to control the stoichiometry and the particle size. Once the fuel is used, its reprocessing to extract burnable uranium and plutonium includes troublesome solution processes using flammable organic solvents. We have focused on hydrothermal synthesis, *i.e.* solid-solution system at temperature of 100-450°C and pressure of 0.1-22 MPa, in order to dispense with flammable organic solvents and to reduce the amounts of radioactive wastes.

The lower dielectric constant of the high-temperature water leads to equilibrium shifts from soluble metallic ions to solid metallic oxides. The supercritical hydrothermal synthesis was widely reported for metallic oxides with fluorite structure such as CeO₂, ZrO₂, HfO₂ and ThO₂. In spite of the lack of experimental reports for AnO₂ (An = U, Np, Pu), the fluorite-type AnO₂ is expected to be produced under the hydrothermal condition.

Figure 1 shows a schematic flow-sheet of the proposed hydrothermal process [1]. The first step is the reprocessing, *i.e.* a removal of fission products from actinides owing to the nature of actinide ions which exclusively form stable coordination compounds with carbonate anion (CO₃²⁻). The

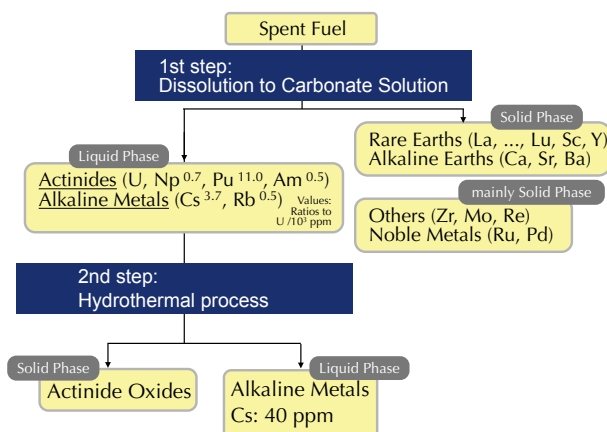


Fig. 1 Hydrothermal process for MOX fuel fabrication and reprocessing.

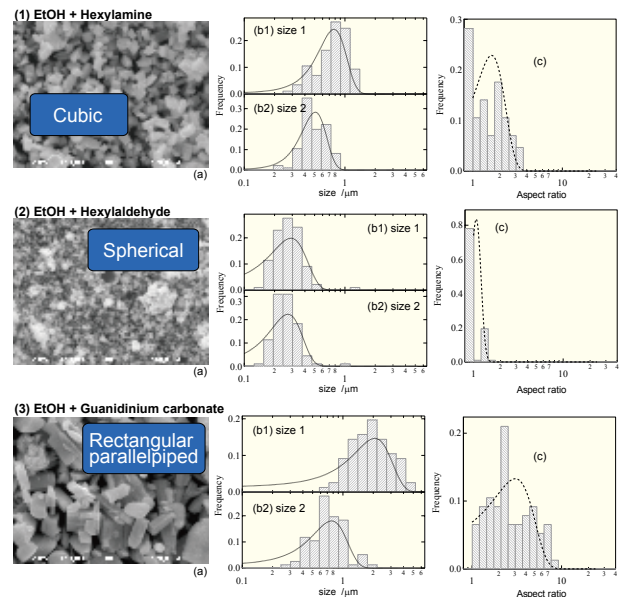


Fig. 2 Shape (a), size (b) and aspect ratio (c) of UO₂ particles obtained by hydrothermal process with two additives.

second step is the combination of the reprocessing and the fabrication of MOX fuel, *i.e.* the hydrothermal process at 450°C for 30 minutes with a reductant. This process separates actinide oxides (MOX fuel) from cesium ion down to 40 ppm. When only ethanol is added as a reductant, the product of UO₂ crystal is indefinite, whereas the second additive such as hexylamine, hexylaldehyde, or guanidinium ammonium alters a fashion how the crystal grows of UO₂, *i.e.* the shape and the size (Fig. 2). Simultaneously, the additives govern the reductive atmosphere and determines the non-stoichiometry *x* of UO_{2+x} in the range of 0.05-0.2. The detailed chemistry in the control of the specifications of AnO₂ is now underway.

References

[1] T. Yamamura, et al., Preparation method of crystals of oxides of actinides, PCT/JP2009/055458 (2009).

Key Words

Stoichiometry, Actinide Dioxides, Crystal Growth

Contact to

Tomoo Yamamura (Radiochemistry of Metals Division)

E-mail: yamamura@imr.tohoku.ac.jp

URL: <http://www.shiokawa.imr.tohoku.ac.jp/>

Production of Ni-Cr-P-B Metallic Glass-coated Bipolar Plate for Fuel Cell by HVOF Spray-coating Method

In this study, the newly designed bipolar plate for proton exchange membrane fuel cells (PEMFC) was produced by spray-coating the $Ni_{65}Cr_{15}P_{16}B_4$ metallic glass on Al plate having a bipolar plate flow field and the electricity generation tests with the single fuel cell having the glass-coated bipolar plates were conducted. As a result, the single cell with the metallic glass-coated bipolar plates showed very high I-V performance as well as the cell with the carbon bipolar plates.

Proton exchange membrane (PEM) fuel cell has been widely recognized as one of the most powerful candidates for near future power generating devices of the automobiles and the home appliances. Bipolar plates are one of the most important components of PEM fuel cells and are multifunctional as they conduct electricity from cell to cell, they separate the fuel gas from the oxidant gas, and their flow field supplies the gases to the electrodes.

Metallic glassy alloys are also potential materials for bipolar plates because they have many advantageous characteristics over crystalline alloys. For example, glassy alloys exhibit higher mechanical strengths and higher corrosion resistance. We have developed the Ni-based metallic glassy alloys suitable for bipolar plate application [1, 2].

In this work, we adopted the high-corrosion-resistant Ni-Cr-P-B metallic glass for bipolar plate production and produced a new metallic glass-coated bipolar plate by the high velocity oxy-fuel (HVOF) spray-coating method and examined the electricity generation properties of the single fuel cell with those metallic glass-coated bipolar plates.

Figure 1 shows the outer view of the $Ni_{65}Cr_{15}P_{16}B_4$ metallic glass-coated Al bipolar plate produced by HVOF spray-coating and subsequent hot-pressing. The glass film was deposited on both sides of the plates.

Figure 2 shows the I-V curves of the single fuel cell with

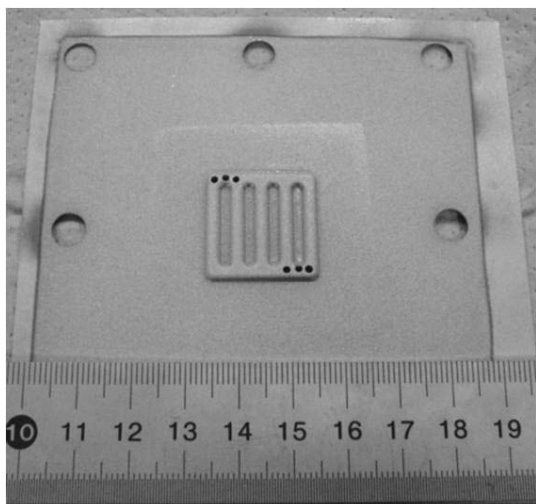


Fig. 1 Outer view of the $Ni_{65}Cr_{15}P_{16}B_4$ metallic glass-coated Al bipolar plate.

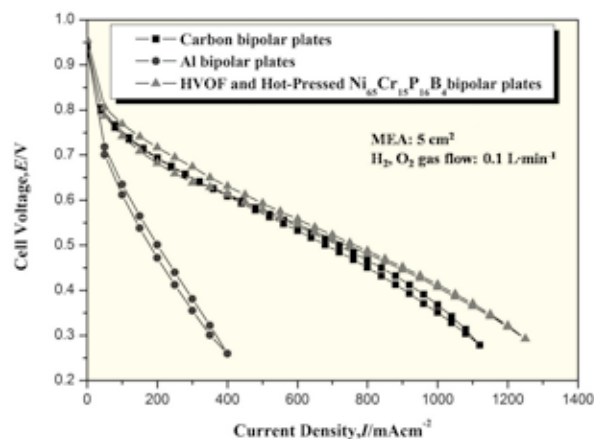


Fig. 2 I-V curves of the single cell with carbon, Al and $Ni_{65}Cr_{15}P_{16}B_4$ metallic glass bipolar plates.

carbon graphite, Al and $Ni_{65}Cr_{15}P_{16}B_4$ glassy alloy bipolar plates measured at the cell temperature of 353 K at the gas flow rate of $0.1 \text{ L} \cdot \text{min}^{-1}$. The results measured after 50 times repetition for aging the membranes were indicated in the figure. At the cell voltage of 0.5V, the single cells employing graphite, Al, and $Ni_{65}Cr_{15}P_{16}B_4$ glassy alloy bipolar plates generated the current density of 700, 200, and 750 $\text{mA} \cdot \text{cm}^{-2}$, respectively. As clearly seen in the figure, the single cell with the $Ni_{65}Cr_{15}P_{16}B_4$ glass-coated bipolar plates showed better I-V performance than that with Al bipolar plates. This is because the Al bipolar plates are easily subjected to corrosion, resulting in the increase in contact electrical resistance. The I-V performance of the single cell with the $Ni_{65}Cr_{15}P_{16}B_4$ glass-coated bipolar plates is as high as that with the carbon graphite bipolar plates. This means that the corrosion resistance of the $Ni_{65}Cr_{15}P_{16}B_4$ metallic glass is so high that it can be applied to bipolar plates in practice.

References

- [1] S. Yamaura, M. Yokoyama, H.M. Kimura and A. Inoue, J. Phys.:Conf. Ser. **144**, 012001 (2009).
- [2] M. Yokoyama, S. Yamaura, H.M. Kimura and A. Inoue, Int. J. Hydrogen Energy **33**, 5678 (2008).

Key Words

Metallic Glass, Bipolar Plate, Fuel Cell

Contact to

Shin-ichi Yamaura (NEDO Laboratory for Metallic Glass Research Collaboration and Promotion)

E-mail: yamaura@imr.tohoku.ac.jp

A New Method for Size Estimation of Cu Nano-precipitates in Fe Based on Positron Quantum-dot Confinement

A new method for size estimation of Cu subnano-precipitates in Fe based on a positron quantum-dot-state is developed. The size of Cu subnano-precipitates which are too small to be detected even by the other technique, such as 3D-AP, can be estimated

The main origin of the embrittlement of the nuclear reactor pressure vessel (RPV) steels due to long-term in-service neutron irradiation is considered to be the (sub) nano-precipitates of Cu contained in the old RPV enhanced by the neutron irradiation. In the early stage of Cu subnano-precipitate formation, it has been difficult to obtain the size of the precipitates even by high-resolution transmission electron microscope or three-dimensional atom probe (3D-AP).

Positrons are confined in Cu subnano-precipitates in Fe by positron affinitive trapping. The positron quantum-dot confinement leads to smearing of positron-electron momentum density distribution around the Fermi cut-off momentum (p_F) as shown in Fig. 1. Due to the uncertainty principle between position and momentum, the momentum smearing is inversely proportional to the size of the quantum-dot. Therefore, we have observed the momentum smearing by two-dimensional angular correlation of positron annihilation radiation (2D-ACAR) and estimated the average size of the Cu nano-precipitates where positrons are confined.

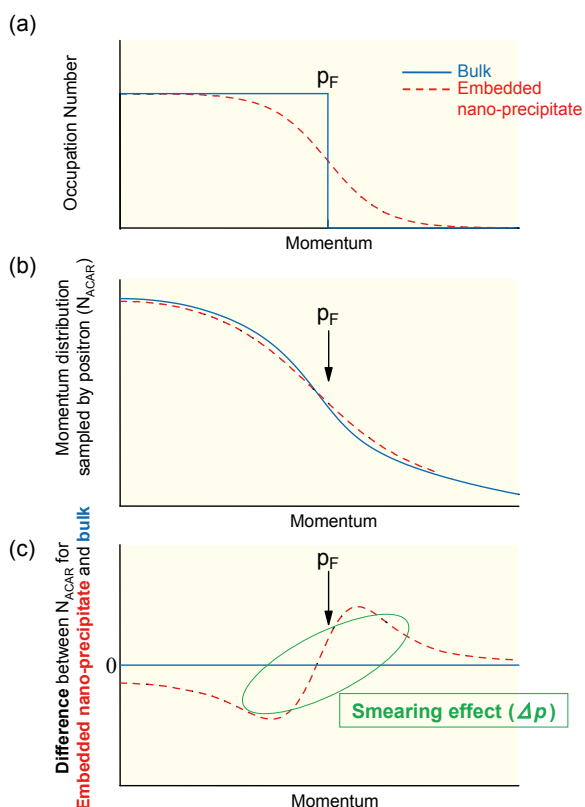


Fig. 1 (a) Electron occupation number around the Fermi momentum, (b) Angular correlation of positron annihilation radiation spectrum (N_{ACAR}), (c) Difference of N_{ACAR} between bulk and embedded nano-precipitate.

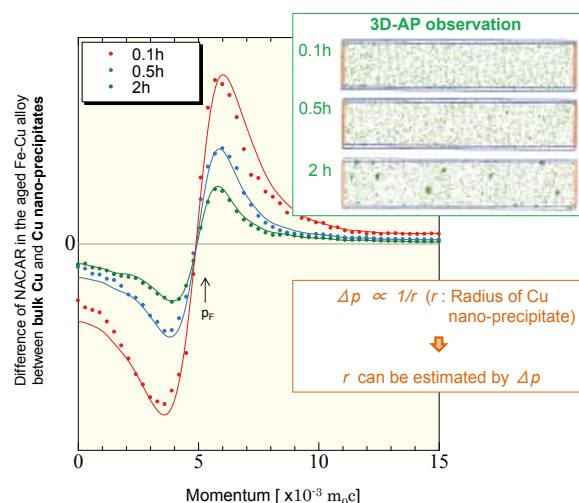


Fig. 2 Difference of N_{ACAR} in the aged Fe-Cu alloy between bulk Cu and Cu nano-precipitate. The smearing effect clearly depends on the aging time, *i.e.*, size of Cu nano-precipitates. The smearing effect (Δp) is assessed quantitatively using the Gaussian function convolution for N_{ACAR} of bulk Cu and then size of Cu nano-precipitate is estimated.

Fe-Cu alloy was aged at 475°C for 0.1 to 20 h to form the Cu nano-precipitates with various sizes. Figure 2 shows the aging time dependency of momentum smearing effect observed by 2D-ACAR. The average sizes of the Cu nano-precipitates were estimated from the smearing effect and then compared with those by 3D-AP as also shown in Fig. 2. Both the results agree with each other for samples aged for 1-20 hours. Furthermore, the present method gives the sizes of the Cu subnano-precipitates which are too small to be detected even by the 3D-AP for samples aged for 0.1-2 hours [1]. Thus it is demonstrated that positron annihilation technique is a powerful tool to estimate the size of Cu subnano-precipitates in the early stage of formation.

Reference

[1] T. Toyama, Y. Nagai, Z. Tang, K. Inoue, T. Chiba, M. Hasegawa, T. Ohkubo and K. Hono, Tetsu to Hagane, **95**, 118, (2009).

Key Words

Embedded Nano-precipitates, Positron Annihilation, Three-dimensional Atom Probe

Contact to

Takeshi Toyama (International Research Center for Nuclear Materials Science)

E-mail: ttoyama@imr.tohoku.ac.jp

URL: <http://www.imr-oarai.jp/>

Intergrown alpha-Type Phase in beta-Type Phase TmAlB₄ Crystal Studied by High-Resolution Electron Microscopy

A TmAlB₄ crystal with a ThMoB₄-type (beta-type) structure phase was studied by electron diffraction (ED) and high-resolution electron microscopy (HREM). A HREM image clearly exhibits an intergrown lamellar structure of an YCrB₄-type (alpha-type) phase in the matrix of the beta-type phase in TmAlB₄ crystal. The lamellar structure can be characterized by a tiling of deformed hexagons, which are a common structural unit in the alpha-type and beta-type structures.

It is well known that the rare-earth metal borides have yielded intriguing systems to study fundamental problems in physics and chemistry [1]. The rare-earth (RE) metal aluminoboride system REAlB₄ has been paid much attention. Recently, multiple magnetic transitions were reported to occur in TmAlB₄ at low temperatures below an antiferromagnetic transition temperature T_N [2]. REAlB₄ crystals have two different structure types; alpha- and beta-type structures. Both phases are built by a unique structural unit, which consists of six heptagonal atomic columns containing edge-shared two pentagons (Fig. 1).

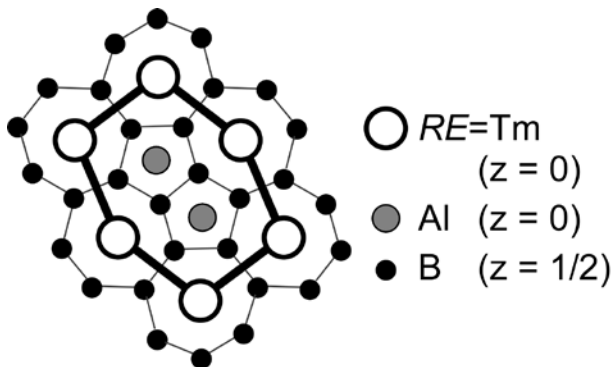


Fig. 1 Structural unit of the deformed hexagon consisting of edge-shared two pentagonal and six heptagonal atomic columns.

In Fig. 2, it is unequivocally demonstrated that an intergrowth nanostructure of the alpha-type phase exists in the beta-type matrix [3]. Based on ED and HREM observations, slivers of the alpha-type “tiling” were clearly observed to be insinuated into the beta-type TmAlB₄ structure. Characteristic diffuse streaks in ED are consistent with the lamellar structure. As can be seen from a tiling, there are coherent interfaces between both phases. The crystallographic relationship between the beta- and the alpha-type phases can be expressed as $(1-10)_{\text{beta}} \parallel (010)_{\text{alpha}}$ and $[001]_{\text{beta}} \parallel [001]_{\text{alpha}}$. The present direct observation of the intrinsic nanostructure indicates that the intergrowth is the origin of low temperature anomalies in the physical properties.

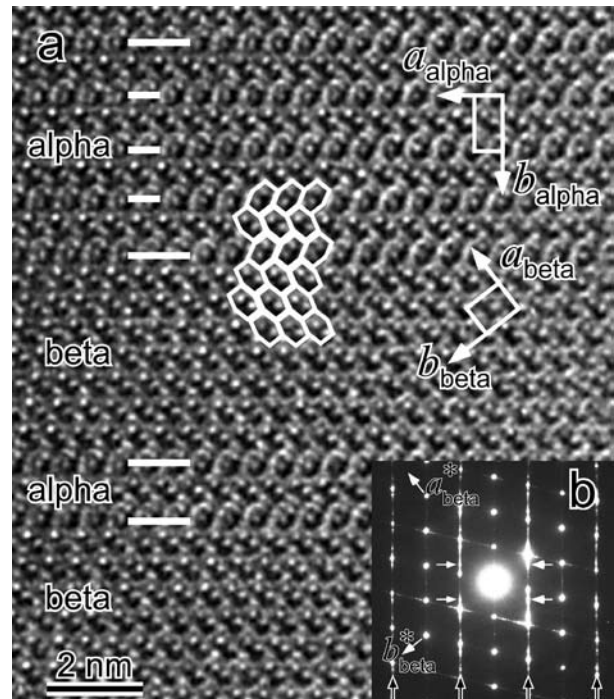


Fig. 2 (a) HREM image and (b) corresponding ED pattern, of an intergrowth nanostructure taken with the incident electron beam parallel to the [001] direction. Deformed hexagons in (a) correspond to the structural unit in Fig. 1.

References

- [1] e.g. T. Mori, "Higher Borides", in: *Handbook on the Physics and Chemistry of Rare Earths*, ed. K. A. Gschneidner Jr., et al., **38**, 105 (2008).
- [2] T. Mori, H. Borrmann, S. Okada, K. Kudou, A. Leithe-Jasper, U. Burkhardt, and Y. Grin, *Phys. Rev. B* **76**, 064404 (2007).
- [3] K. Yubuta, T. Mori, A. Leithe-Jasper, Y. Grin, S. Okada and T. Shishido, *Mater. Res. Bull.*, **44**, 1743 (2009).

Key Words

Rare Earth Aluminoboride, Intergrowth Structure, Electron Microscopy

Contact to

Kunio Yubuta (Advanced Research Center of Metallic Glasses)
E-mail: yubuta@imr.tohoku.ac.jp

Cryogenfree 23 T Superconducting Magnet with a 7.5 T YBa₂Cu₃O₇ Insert

In order to develop a cryogenfree high-field superconducting magnet generating over 20 T, a Y123-coated conductor insert is used to enhance a cryogenfree 18 T superconducting magnet. The Y123 tape does not require stainless steel reinforcement. The Y123 insert, which is almost the same size as the current Bi2223 insert, is designed to generate 7.5 T at 187 A. It is able to achieve this since without stainless steel reinforcement the number of turns can be greatly increased. A cryogenfree superconducting magnet can achieve a static magnetic field of 23 T, which is higher than that generated by practical superconducting magnets using liquid helium.

Static high-field facilities around the world require huge electrical powers in the range 20 to 30 MW to power a water-cooled resistive magnet of a hybrid magnet system. It is difficult for university laboratories to afford such high electricity costs. Superconducting technology is essential for constructing high static field facilities that do not consume huge amounts of power. We introduce an improvement to the cryogenfree superconducting magnet that involves incorporating an YBa₂Cu₃O₇ (Y123) coated conductor tape and enables the magnet to generate a high static field of 23 T.

We focus on the larger critical current density of YBa₂Cu₃O₇ (Y123) coated conductors than that of Bi2223 tape at 4.2 K. When we employ the new insert fabricated with high performance Y123 conductors, higher magnetic fields over 20 T can be targeted. Although the splendid J_c properties in strong magnetic fields over 20 T for $B//c$ is difficult even for the Y123 superconductor, the magnetic field applied to an insert in a background magnet is almost parallel to the superconducting tape surface. This means that the c-axis-parallel component is quite small in the insert in background fields. We understand that the critical current characteristic in the c-axis-perpendicular field component for Y123 is far excellent, when Bi2223 and Y123 are compared each other. Figure 1 shows the I_c - B characteristics for Bi2223 and Y123 at 4.2 K. Y123 coated conductors developed as practical long-length 4 mm wide and 0.1 mm thick tapes have the I_c

Table I Comparison of the Bi2223 insert for 18T-CSM and the Y123 insert for 23T-CSM

Superconductor		Bi2223	Y123
Supercond. tape size	mm ²	4.3 × 0.21	4.0 × 0.1
Cowinding reinforcement	mm	SUS 0.3	Hastelloy 0.05
Inner diameter	mm	90	90
Outer diameter	mm	176	176
Coil height	mm	252	252
No. of layers		50 (25 DP)	50 (25 DP)
Total turns		3548	9350
Operation current	A	161	187
Central field (15.6 T backup)	T	18.1	23.3
Hoop stress	MPa	98	439

value of 80 A at 77 K in a self-field. It was found that the Y123 has splendidly high I_c potentials in fields for both $B//c$ and $B\perp c$ directions to design the insert with high current densities. The coil load lines are well determined to generate 23 T for $B\perp c$. In this case, we understand that the c-axis-parallel field component is 3.1 T.

Table I lists the design parameters for the Y123 insert coil of the 23 T cryogenfree superconducting magnet (23T-CSM). The coil current density was increased by a factor of over three from 50 to 160 A/mm² by replacing the Bi2223 coil with the Y123 one. Reinforcement is reduced from 0.3-mm-thick stainless steel tape to 0.1-mm-thick Hastelloy tape including the coated conductor substrate. The Y123-coated conductor tape with Hastelloy reinforcement can overcome huge electromagnetic stresses of up to 1000 MPa. Therefore, it is expected that the Y123 tape can withstand the electromagnetic force of 440 MPa in the 23T-CSM. This means that stainless steel reinforcement is no longer required for the insert coil. As a result, a Y123 insert coil of almost the same size as the Bi2223 insert coil will generate 7.5 T at 187 A, because the number of turns without stainless steel reinforcement can be greatly increased. A cryogenfree superconducting magnet can achieve a 23 T static magnetic field in a 52 mm experimental bore at RT [1].

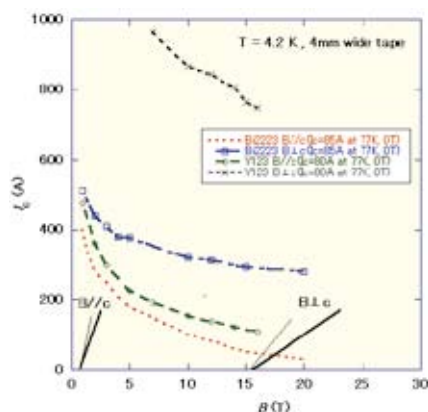


Fig. 1 Comparison of the I_c properties at 4.2 K in fields for $B\perp c$ and $B//c$ between Ag-sheathed Bi2223 tape (Sumitomo Electric Co.) and Y123 coated conductor tape (SuperPower Co.).

References

[1] Superconducting Magnet with a 7.5 T YBa₂Cu₃O₇ Insert Coil, K. Watanabe, S. Awaji, G. Nishijima, S. Hanai and M. Ono, Appl. Phys. Express 2, 113001 1-3 (2009).

Key Words

Y123 Coated Conductor, High Field, Cryogenfree Superconducting Magnet

Contact to

Kazuo Watanabe (High Field Laboratory for Superconducting Materials)

E-mail: kwata@imr.tohoku.ac.jp

URL: <http://hflsm.imr.tohoku.ac.jp>

Promotional Effect of Au/Pd Bimetallic Nanoparticles for Photocatalytic Activities

Au/Pd bimetallic nanoparticles were successfully prepared from aqueous solution of the corresponding noble metal salts and immobilized on TiO₂ by the effect of high-power ultrasonic irradiation. These nanoparticles exhibited unique promotional effect for TiO₂ photocatalysis depending upon the inner nanostructure even if they had same content of Au/Pd ratio.

Designing nano-morphologies is expected to be one of the promising approaches to develop the novel high performance catalysts. The author reported the preparation of bimetallic nanoparticles consisting of Au-core and Pd-shell using unique methodology utilizing the high energy reaction sites induced by high power ultrasonic irradiation [1]. The inner structures of alloy nanoparticles such as core/shell structure have been receiving increasing attention to enhance the catalytic activities of the particles with high performance as compared with that of the constituent metals. In this study, the photocatalytic activities of TiO₂ supporting Au/Pd bimetallic nanoparticles prepared by ultrasonic irradiation were evaluated.

Au-core/Pd-shell bimetallic nanoparticles dispersions were prepared by the previously reported sonochemical method [1]. TiO₂ (P-25) was added to the dispersion of the nanoparticles, and followed by the sonication (200 kHz, 6 W/cm²) under air atmosphere to immobilize noble metal nanoparticles on the surface of TiO₂ (sample A) [2].

According to the HAADF-STEM image, nanosized Au-core/Pd-shell nanoparticles with multiple twined structure were confirmed to be immobilized on TiO₂ surface (Fig. 1(a)). The mixtures of Au and Pd monometallic nanoparticles individually prepared were also immobilized by the same procedure (sample B). On the other hand, by annealing sample A, the core/shell structure was broken and changed into ordered state where Au and Pd atoms were homogeneously located in each particle (sample C, shown in Fig. 1 (b)) [3]. Neither sintering of the supported nanoparticles nor growth in their sizes was not observed after the annealing. ICP analyses showed that the contents were similar between sample A, B, and C.

Photocatalytic H₂ evolution was employed for evaluation

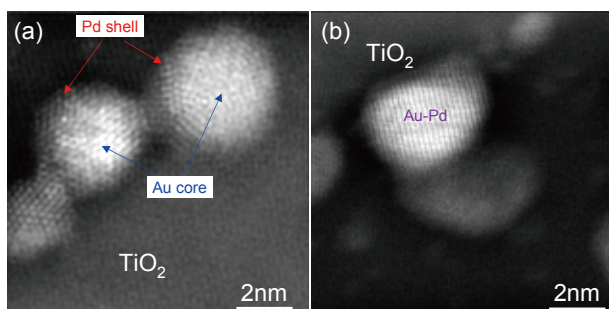


Fig. 1 HAADF-STEM images of (a) as prepared and (b) annealed Au/Pd bimetallic nanoparticles immobilized on TiO₂.

Table 1 H₂ evolution by sonochemically prepared photocatalysts

Sample	H ₂ / mmol (h-g-cat (mW·cm ⁻²)) ⁻¹	
	UV illumination ^a	Vis illumination ^b
A (Au-core/Pd-shell)	140.0	17.4
B (Au-Pd mixture)	74.7	10.2
C (Annealed)	213.1	13.0

^a 250 – 385 nm. ^b 385 – 740 nm.

for the samples. Ar-purged ethanol aqueous solutions containing the prepared photocatalysts were illuminated by a Xe lamp in a closed glass vessel with a quartz window. The amounts of evolved H₂ depended on the wavelength of the illuminated light and the nanostructure of the supported nanoparticles (Table 1). These results indicate that the bimetallic nanoparticles (samples A and C) effectively trap the photo-excited electrons compared with the mixture (sample B). Moreover, XPS studies suggested the change in the band structures depending on the inner structures of the immobilized bimetallic nanoparticles [4].

These results suggest that designing inner structure of the bimetallic nanoparticles provides new functions differing from intrinsic features of constituting elements.

References

- [1] Y. Mizukoshi, T. Fujimoto, Y. Nagata, R. Oshima, Y. Maeda, *J. Phys. Chem. B*, **104**, 6028-6032 (2000).
- [2] Y. Mizukoshi, Y. Makise, T. Shuto, J. Hu, A. Tominaga, S. Shironita and S. Tanabe, *Ultrason. Sonochem.*, **14**, 387-392 (2007).
- [3] T. Nakagawa, H. Nitani, S. Tanabe, K. Okitsu, S. Seino, Y. Mizukoshi and T. A. Yamamoto, *Ultrason. Sonochem.*, **12**, 249-254 (2005).
- [4] Y. Mizukoshi, K. Sato, T. J. Konno and N. Masahashi., *Appl. Catal. B Environ.*, **94**, 248-253 (2010).

Key Words

Catalyst, Bimetallic Nanoparticle, Ultrasound

Contact to

Yoshiteru Mizukoshi (Osaka Center for Industrial Materials Research)

E-mail: mizukosi@imr.tohoku.ac.jp

URL: <http://polar.imr.tohoku.ac.jp>